Moth wings are acoustic metamaterials

Thomas R. Neil[a,1], Zhiyuan Shen[a,1], Daniel Robert[a], Bruce W. Drinkwater[b], and Marc W. Holderied[a,2]

[a]School of Biological Sciences, University of Bristol, Bristol BS8 1TQ, United Kingdom; and [b]Department of Mechanical Engineering, University of Bristol, Bristol BS8 1TR, United Kingdom

Edited by Katia Bertoldi, Harvard University, Cambridge, MA, and accepted by Editorial Board Member Evelyn L. Hu October 4, 2020 (received for review July 10, 2020)

Metamaterials assemble multiple subwavelength elements to create structures with extraordinary physical properties (1–4). Optical metamaterials are rare in nature and no natural acoustic metamaterials are known. Here, we reveal that the intricate scale layer on moth wings forms a metamaterial ultrasound absorber (peak absorption = 72% of sound intensity at 78 kHz) that is 111 times thinner than the longest absorbed wavelength. Individual scales act as resonant (5) unit cells that are linked via a shared wing membrane to form this metamaterial, and collectively they generate hard-to-attain broadband deep-subwavelength absorption. Their collective absorption exceeds the sum of their individual contributions. This sound absorber provides moth wings with acoustic camouflage (6) against echolocating bats. It combines broadband absorption of all frequencies used by bats with light and ultrathin structures that meet aerodynamic constraints on wing weight and thickness. The morphological implementation seen in this evolved acoustic metamaterial reveals enticing ways to design high-performance noise mitigation devices.

biosonar | acoustics | ultrasonic | moth scale | natural metamaterial

Nocturnal lepidoptera (moths) are under intense evolutionary pressure from echolocating bats, which has led to a host of bat avoidance strategies (7), including ultrasound sensitive hearing to detect and escape from foraging bats (8, 9), and the production of ultrasonic clicks to confuse or warn attacking bats (10, 11). Many moth species, however, do not possess ultrasound-sensitive ears and instead rely on other defense mechanisms. One such defense is acoustic camouflage, whereby ultrasound backscatter has evolved to reduce detectability by bat biosonar.

In flight, for example, a thick fur-like scale layer protects moth bodies from bat detection by serving as porous absorber of bat ultrasound (6). The fluttering wings of moths also have the potential to reflect strong echoes (6), yet they are covered in an aerodynamically constrained much thinner tiling of paddle-shaped scales (Fig. 1*A*), which provides thermoregulation (12), anti-stick coating (13), and visual camouflage (14), with some evidence for rudimentary sound absorption (15). Here, we document a comprehensive, biologically relevant acoustic functionality of these wing scales: the ability to provide stealth acoustic camouflage by acting as an ultrathin yet broadband sound-absorbing metamaterial.

Moth Wings Are Deep-Subwavelength Broadband Sound Absorbers

Circular sections (⌀ 6 mm) were punched out from leading and trailing edge regions of intact dried forewings of two earless moth species, *Antheraea pernyi* (Saturniidae) and *Dactyloceras lucina* (Brahmaeidae), and two butterfly species, *Graphium agamemnon* (Papilionidae) and *Danaus chrysippus* (Nymphalidae) (Fig. 1*A*). Echoes reflected by these samples with and without scales were quantified for normal (perpendicular) sound incidence, establishing their target strength (reflected vs. incident sound intensity) as a function of frequency (Fig. 1 *B* and *C*).

Scale removal changed the target strength significantly for the frequency range many bat species use for the detection of flying prey (20 to 60 kHz) across species and wing regions [$F_{(7,32)} = 13.45$, $P < 0.001$; Fig. 1*B*]. In moths, the presence of scales reduced the mean target strength in both wing regions by −3.51 ± 1.02 and −4.80 ± 0.61 dB in *A. pernyi* and by −3.03 ± 0.69 and −5.02 ± 1.09 dB in *D. lucina*. Because only small fractions of the incident sound are transmitted or diffused (*SI Appendix*, Figs. S1 and S2), this reduction in target strength can be attributed to absorption (absorption coefficient α). In contrast, in both butterfly species, the presence of scales increased the mean target strength by 0.53 ± 0.44 and 1.10 ± 0.67 dB on the two wing regions in *G. agamemnon* and by 1.56 ± 0.81 and 1.31 ± 0.73 dB in *D. chrysippus* (Fig. 1*B*). Similar effects were found over the full frequency range from 20 to 160 kHz (Fig. 1*C*).

Scanning electron microscopy (SEM) and micro-computed tomography (micro-CT) data showed that scales on moth wings form a soft layer that is generally less than 0.3 mm thick (Fig. 1*A* and *SI Appendix*, Table S1), which is much thinner than the acoustic wavelengths, λ, that bats use for echolocation (e.g., λ = 17 mm at 20 kHz). Wings create their strongest echoes when ensonified perpendicularly (6), so we investigated the scales' absorptive performance for normal sound incidence. The ratio between this wing thickness, T, of moths and the wavelength of sound (over 20 to 160 kHz; Fig. 1*C*) was found to range from 1/111 to 1/5. Peak target strength reduction for the leading and trailing wing areas was −4.42 dB ($\alpha = 0.64$ at $T/\lambda = 1/100$) and −5.15 dB ($\alpha = 0.69$ at $T/\lambda = 1/33$) in *A. pernyi* and −3.14 dB ($\alpha = 0.51$ at $T/\lambda = 1/50$) and −5.50 dB ($\alpha = 0.72$ at $T/\lambda = 1/13$) in *D. lucina*. In comparison, the scale layer on butterfly wings is thinner (Fig. 1*A*) and either has very little effect or even increases the reflection coefficient (Fig. 1*C*). In short, scales on moth wings demonstrably absorb much of the impinging acoustic

Significance

Bats and moths are embroiled in an evolutionary arms race. Using ultrasonic biosonar, bats detect their insect prey, which in turn deploy diverse strategies to avoid predation. Here, we show that some moth species evolved wings covered with a canopy of scales that reduces ultrasonic echoes. Our empirical and mathematical analysis together show that moth wings exhibit key features of a desirable technological acoustic metamaterial. This work enriches our understanding of the structural and functional complexity of lepidopteran wings and reveals enticing new ways to design, using bioinspired metamaterial properties, high-performance acoustic panels and noise mitigation devices.

Author contributions: T.R.N. and M.W.H. designed research; T.R.N., Z.S., and M.W.H. performed research; D.R., B.W.D., and M.W.H. contributed new reagents/analytic tools; T.R.N., Z.S., D.R., B.W.D., and M.W.H. analyzed data; and T.R.N., Z.S., D.R., B.W.D., and M.W.H. wrote the paper.

The authors declare no competing interest.

This article is a PNAS Direct Submission. K.B. is a guest editor invited by the Editorial Board.

[1]T.R.N. and Z.S. contributed equally to this work.

[2]To whom correspondence may be addressed. Email: marc.holderied@bristol.ac.uk.

This article contains supporting information online at https://www.pnas.org/lookup/suppl/doi:10.1073/pnas.2014531117/-/DCSupplemental.

First published November 23, 2020.

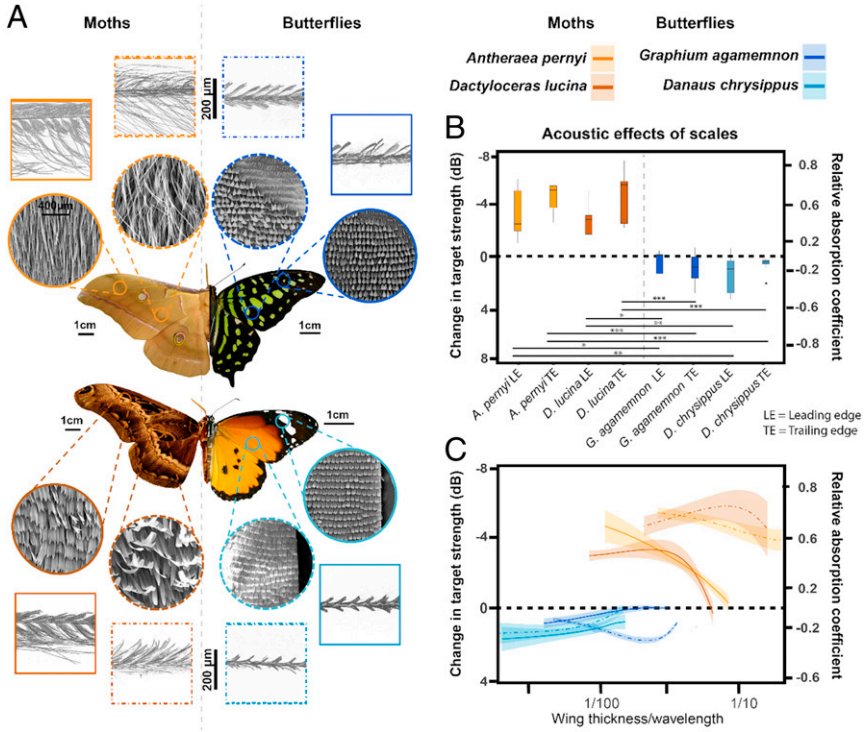

Fig. 1. Tiling patterns and acoustic effects of lepidopteran scales. (*A*) Photographs of butterflies *Graphium agamemnon* and *Danaus chrysippus,* and moths *Dactyloceras lucina* and *Antheraea pernyi* (clockwise from *Top Right*). Circles indicate sampling positions on leading and trailing regions of forewings. Round *Insets* show SEM images of dorsal surfaces, and square *Insets* show micro-CTs of cross sections of each wing sample. (*B*) Change in target strength (integrated over 20 to 60 kHz at normal sound incidence) caused by presence of scales, and equivalent intensity absorption coefficient (boxplots show median, interquartile range, and 95% confidence intervals; $n = 5$). Horizontal lines show pairwise comparisons with $^{*}P \leq 0.05$, $^{**}P \leq 0.01$, and $^{***}P \leq 0.001$. (*C*) Change in target strength (for 20 to 160 kHz at normal sound incidence) caused by presence of scales, and equivalent absorption coefficient as a function of wing thickness/wavelength. Solid and stippled colored lines are average values; associated shaded areas show ± SD ($n = 5$).

energy, and do so over the range of biologically relevant frequencies, thereby reducing detection risk by bat echolocation. Remarkably, moth scales absorb sound down to the lowest frequencies tested (20 kHz) providing deep-subwavelength absorber functionality.

Moth Wings as Broadband Resonant Acoustic Metamaterial

Such highly desirable deep-subwavelength acoustic functionality is not easily attained. For example, the porous absorbers typically used in sound insulation require significantly increased thickness to reach this level of absorption (16). Resonant absorbers, however, can operate at such low thickness to wavelength ratios (16), and they are most efficient at their resonance frequency (17). Remarkably, single moth scales exhibit resonances within the frequency range used by bats (5), potentially offering resonant absorber functionality. The inherent drawback of resonant absorbers is that they only absorb sound in the narrow band of their resonance frequency (5). This raises the question of what mechanism moth wings evolved to get the best of both worlds—deep-subwavelength thickness and broadband absorption.

In laboratory experiments, researchers have used arrays of differently tuned resonators to achieve broadband acoustic absorption (1, 18); one broadband optimal metamaterial absorber (BOMA) consisting of 16 different Fabry–Perot resonators achieves a near-perfect absorption spectrum down to $T/\lambda = 1/9$. Because of their resonant functionality (5) and tiled arrangement (Fig. 1*A*), we propose that moth wing scales constitute a biological metamaterial absorber (BioMA). We test this using a combination of empirical and numerical analysis of scale array resonances and vibroacoustic modeling of their absorptive metamaterial performance.

Scale Layers as Resonator Arrays: Measurements

The distribution of resonant frequencies of a BOMA's elements determines what frequency range they absorb collectively (17). We mounted wing samples onto a cylindrical piezoelectric ultrasound transducer and measured vibrational transfer functions with a scanning laser Doppler vibrometer. Resonance frequencies were identified as maxima in the spectral transfer functions for each scan point (*SI Appendix*, Fig. S3). Remarkably, and as expected for a BOMA, measured collective resonances were distributed evenly across the entire bandwidth tested (20 to 160 kHz) in both moth species (Fig. 2 *A*–*D*).

Scale Layers as Resonator Arrays: Numerical Modeling

Because each scale's morphology determines its resonances (5), the diversity of scale morphology should reflect the observed collective resonance distribution. Scales on the tested lepidopteran wings belong to two types: short base scales that form an underlying tiling pattern and longer cover scales that overlap them (Fig. 1 *A*, *Left*). Moth scales exhibit high shape and size variability depending on scale type, wing region, and dorsal or ventral wing surface (Fig. 1 *A*, *Left*, and *SI Appendix*, Table S1). By contrast, butterfly scales have a distinct paddle shape that varies little across wing regions and between base and cover scales (Fig. 1 *A*, *Right*, and *SI Appendix*, Table S1).

To quantify how each scale's shape (length and width) affects its resonances, finite element models (COMSOL Multiphysics v.5.3a; COMSOL) of single scales were built. Each scale was modeled as a flat plate with the thickness and stalk dimensions typical for each species (Fig. 2 *I* and *J* and *SI Appendix*, Table S2), and key material properties were based on the effective

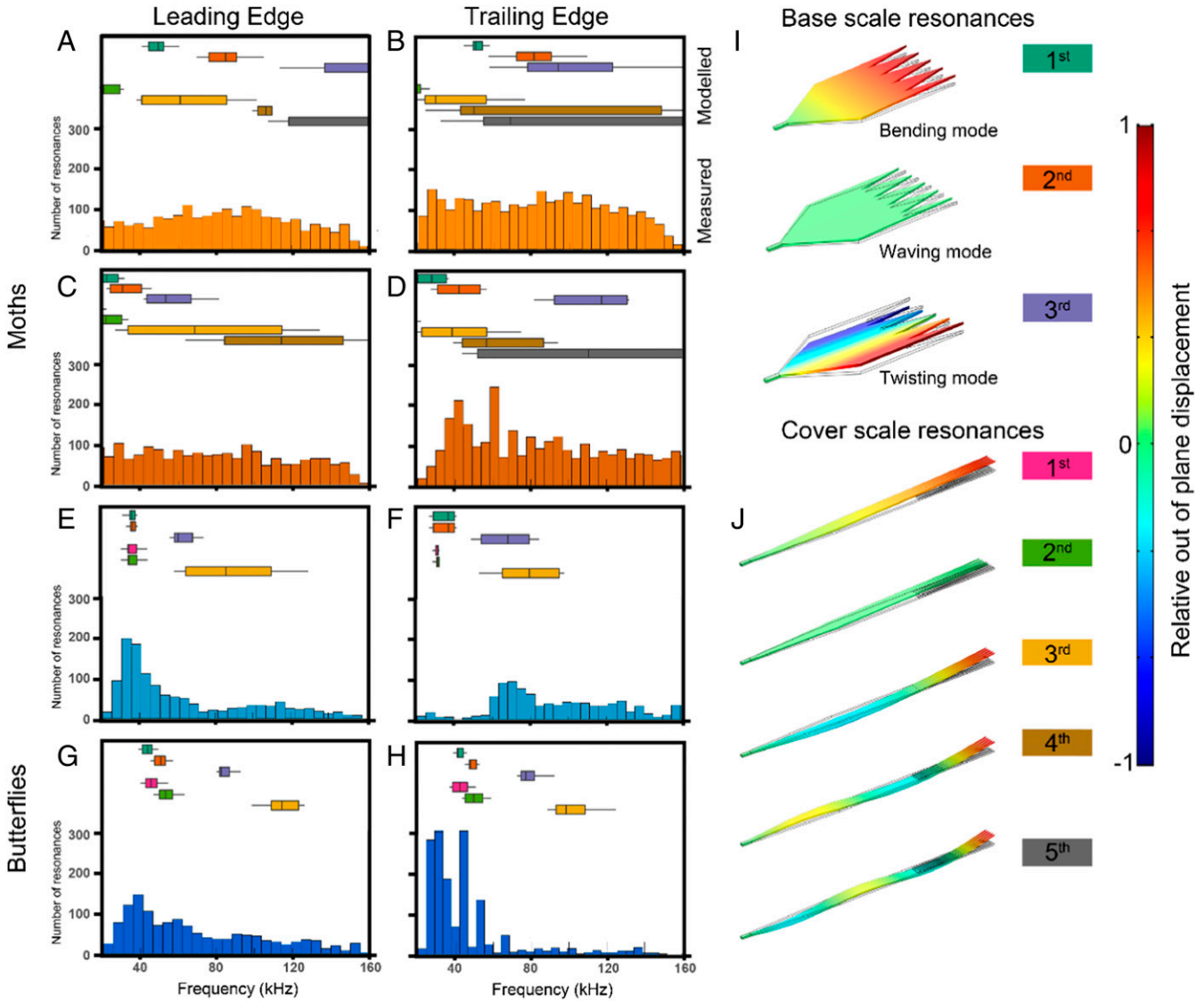

Fig. 2. Empirical and numerical characterization of resonant frequencies of scales on moth and butterfly wings. *A–H* show data from either leading (*A*, *C*, *E*, and *G*) or trailing (*B*, *D*, *F*, and *H*) wing regions of two moths *Antheraea pernyi* (*A* and *B*) and *Dactyloceras lucina* (*C* and *D*), and two butterflies *Danaus chrysippus* (*E* and *F*) and *Graphium agamemnon* (*G* and *H*). (*A–H*, histograms) Distribution of resonant frequencies of scales on an intact 2 × 2-mm area on the dorsal wing as measured by laser Doppler vibrometry. (*A–H*, boxplots) Distribution of frequencies of first to fifth resonance modes calculated for a representative sample of individual scale morphologies (10 base scales and 10 cover scales each) encountered on these wing areas (boxplots show median, interquartile range, and 95% confidence intervals; $n = 10$). (*I* and *J*) Normalized displacement visualizations of calculated resonance modes of (*I*) base scales and (*J*) cover scales. Color of boxes next to depicted resonance modes link each mode to the respective boxplots in *A–H*.

stiffness matrix reported in ref. 5. We created models for 160 individual scales (10 base and 10 cover scales randomly selected from the dorsal surface of leading and trailing wing regions of the four species; *SI Appendix*, Table S1) and calculated the resonance distributions of these scale populations (Fig. 2 *A–H*, boxplots). Most resonances were bending modes, with only the second mode in both scale types exhibiting a left–right swaying (waving) mode and the base scale showing a twisting third mode (Fig. 2 *I* and *J*).

Measured and modeled scale array resonance distributions agree well (Fig. 2). Specifically, the first three resonance modes of moth base scales and four to five modes of moth cover scales were all at biosonar frequencies, creating a remarkably even distribution of measured resonances, and altogether covering the full bat frequency range (Fig. 2 *A–D*). This broad resonant frequency distribution mirrors the measured broadband absorption spectra (Fig. 1*C*), which supports our proposition that moth wings act as a BioMA. Butterfly wing scales, on the other hand, resonated preferentially in certain frequency clusters (Fig. 2 *E–G*): In *D. chrysippus* around 36 and 72 kHz on leading and trailing regions, respectively (Fig. 2 *E* and *F*), and in *G. agamemnon* around 40 and 35 kHz (Fig. 2 *G* and *H*). Numerical modeling placed the first three modes of butterfly scales in the biosonar range, but mainly in limited frequency clusters, which mirrors the clusters seen in the measured resonance data (Fig. 2 *E–H*). However, the resonance clusters in butterflies do not create matching absorption peaks, showing that scale resonance is necessary but not sufficient to create absorption. The higher diversity and complexity of moth scaling architecture (Fig. 1*A* and see ref. 5) seem to play a decisive role.

Mixed Scale Arrays as Acoustic Metamaterials

Numerical modeling of a simplified scale array confirms that the remarkable acoustic properties of moth wings (Fig. 1) emerge

from the interaction of differently tuned single scale resonators coupled via a shared flexible membrane. The model contains a four-by-four array of scales with stalks inserted into a wing membrane (Fig. 3, *Right Inset*). Scale shape, size, orientation, overlap, and scale and membrane thickness were modeled after real moth wings (*SI Appendix*, Table S1), and scales and wing membrane were assigned an empirical effective stiffness matrix and constant damping loss factor of 0.045 (5). A metamaterial absorber must incorporate some damping to smooth out gaps between individual resonant peaks. Engineered BOMAs use an additional porous damping layer (18), whereas damping is an integral aspect of moth scale morphology and materials (5). To test the capacity of such arrays of mixed scales on a flexible membrane to produce emergent acoustic phenomena, we generated a simplified but quantitative model, where instead of using differing scale lengths and widths as seen in moth wings, resonance tuning was realized by applying a scaling factor to the stiffness matrix of otherwise-identical scales.

Displacement spectra of individual scales in this model changed in response to the stiffness of neighboring scales (*SI Appendix*, Fig. S5), showing that neighboring scales on a shared flexible membrane are coupled and mutually affect each other's vibroacoustic responses. The specific arrangement of (neighboring) resonators within engineered metamaterials is known to shape their acoustic functionality. Spatially graded resonator arrays can create bandgap widening (19), rainbow trapping (20–22), and acoustic mode conversion effects (23, 24). The scales and tiling patterns on moth wings also show morphological gradation from the base to the apex of the wing, but the functional significance of this remains unknown. Spatially disordered arrangement of resonators can further widen the bandgap compared to graded configurations (19, 25).

To evaluate the ability of an array of 16 differently tuned resonators to create broadband absorption, stiffness scaling factors of the 16 scales were set to create first mode resonances from 30 to 45 kHz at 1-kHz intervals reaching deep-subwavelength dimensions ($T/\lambda = 1/60$ to $1/87$). There are many ways of arranging 16 scales, and we arbitrarily chose a pandiagonal magic square, where the central frequencies on each row, column, diagonal, and pandiagonal have the same sum of 150 kHz (Fig. 3, *Right Inset*). Perfectly matched layers at the top and bottom of the model absorb sound waves such that the air surrounding the scales was effectively infinite. The side walls of the model were made periodic boundaries, which expands the 16-scale array into an infinite two-dimensional (2D) array. Infinite size was assumed for conceptual simplicity because entire moth wings typically are several wavelengths in length and width and thus governed by classical diffraction theory. The planar incident sound wave originates from the top, and the absorption of the array was calculated as the difference between the incident wave power and the sum of transmitted and reflected power.

The thin colored lines in Fig. 3 show absorption spectra of resonator arrays with unit cells composed of 16 identical scales. These arrays of identical scales generate a single absorption peak that shifts toward higher frequencies as the stiffness increases. The absorption spectrum of the mixed resonator array (bold black line in Fig. 3) is significantly wider in bandwidth and has a higher absorption peak and a much larger area under the curve than any uniform scale array. These features signify that the interaction between differently tuned scales creates emergent acoustic performance beyond that of its elements, confirming broadband metamaterial absorber functionality for the mixed scale arrays modeled after moth wings. Absorption coefficients calculated using this simplified model ($\alpha \leq 0.47$ at $T/\lambda = 1/69$ to $1/100$) were somewhat lower than those measured from real moth wings (Fig. 1 *B* and *C*), and a more naturalistic model that includes a cover scale layer is likely to achieve such higher absorption. Genetic algorithms to optimize array disorder have been used to purposefully attenuate waves at target frequencies (21), suggesting that similar approaches would also allow higher absorption at target frequencies for scale arrays. A deeper

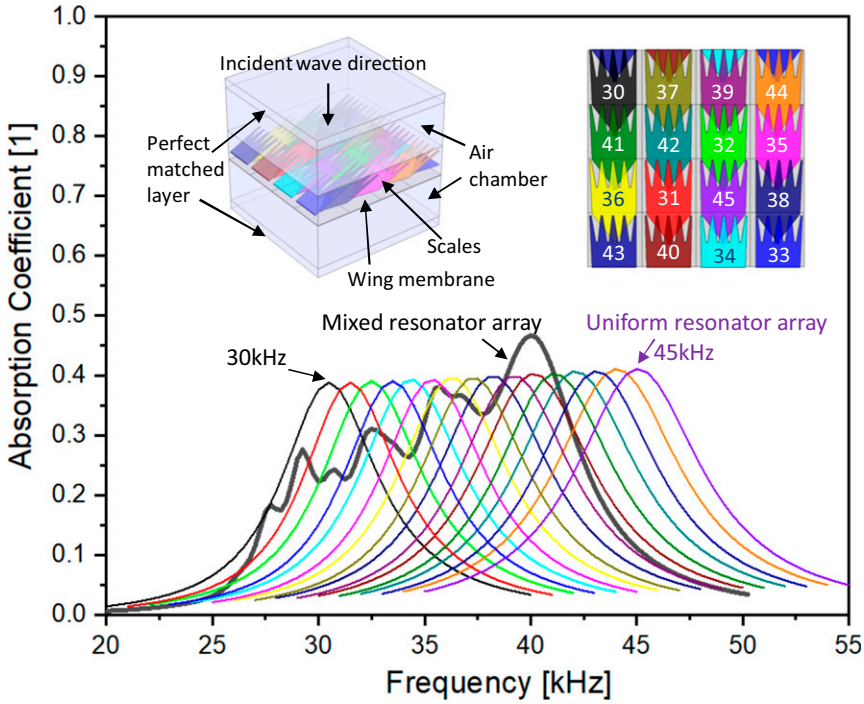

Fig. 3. Calculated absorption spectra of uniform and mixed scale resonator arrays. Colored thin lines: calculated absorption spectra of 16 uniform arrays each composed of 16 identical resonators. Numbers in the *Right Inset* link line colors to the central frequency (in kilohertz) of the corresponding absorption peak. Black bold line: absorption spectrum of the pandiagonal magic square mixed resonator array depicted in the *Right Inset*. (*Right Inset*) Scale arrangement and frequency distribution (numbers in kilohertz) of the mixed resonator array. (*Left Inset*) Schematic of the 3D model used for numerical modeling.

understanding of the biomechanical interaction between neighboring scales will help reveal how the diverse scale morphologies and tiling patterns seen in different moth species create specific acoustic functionality that matches their respective ecological needs.

From BOMA to BioMA

The key design principle shared between engineered BOMAs and moth wings is that they are arrays of resonant elements spanning the frequency bandwidth over which absorption is required. So structurally and conceptually, moth scale layers have the core attributes of metamaterials. Our moth-inspired model confirms that the resonator geometry of moth wings—which is unlike anything considered to date—explains this metamaterial absorber functionality. By inference, we conclude that moth wings achieve their remarkable acoustic performance by scale morphologies and tiling patterns that collectively constitute a BioMA.

Comparing moths with butterflies, which are not under predation pressure by bats and have no sound absorptive properties, sheds light on some relevant morphological adaptations. Moth scales are acoustically well matched to air as the volume-fraction of material (chitin) to air in the scale layer is extremely low (9% and 17% in *D. lucina* and *A. pernyi*, respectively; *SI Appendix*, Table S3) such that sound energy is readily coupled into them (5). The moth scales' low mass in combination with a relatively high stiffness moves their main resonances into the ultrasonic frequency range, where each scale's resonant frequency is tunable by its length, width, stalk stiffness, and angle of insertion into the wing membrane. Butterfly wing scales, in contrast, have a higher volume-fraction (30% in *G. agamemnon* and *D. chrysippus*; *SI Appendix*, Table S3) so are less well coupled acoustically. A metamaterial absorber built with the uniform butterfly scales with their clustered resonances would not provide the wideband absorption arising from the collective action of the morphologically diverse and more broadly tuned moth scales.

In summary, a moth's BioMA provides a form of acoustic stealth camouflage by reducing its echo strength and hence detectability by echolocating bats. We hypothesize that this is a result of predation pressure from bats that use a wide range of frequencies, hence necessitating broadband acoustic camouflage as an evolutionary response. To fulfill a range of other functions including flight, the scale must perform within aerodynamic constraints that limit the thickness and weight of the moth scale layer. Altogether, these evolutionary constraints have resulted in the observed deep-subwavelength metamaterial functionality on the wings, which complements the acoustic protection granted by porous absorbers on the moths' bodies (6). Deep-subwavelength metamaterial sound absorber technology has attracted increasing attention in the past decade, whereby artificial, usually geometrically complex materials are composed of repetitive resonant units. Our study demonstrates that functional implementations of this have existed in nature well before modern science. Understanding these structures and mechanisms offers the future possibility of developing thinner and lighter noise control materials and devices.

Materials and Methods

Lepidoptera Sourcing. We selected large moth species from two families that lack the ability to hear bat calls: one Saturniidae (*Antheraea pernyi*, Guérin-Méneville; mean wing span, 17.0 ± 1.4 cm) and one Brahmaeidae (*Dactyloceras lucina*, Drury; mean wing span, 17.8 ± 0.5 cm). The butterflies for comparison were one Papilionidae (*Graphium agamemnon*, Linnaeus; mean wing span, 10.6 ± 0.5 cm) and one Nymphalidae (*Danaus chrysippus*, Linnaeus; mean wing span, 7.2 ± 0.2 cm), with five specimens representing each species. *A. pernyi* and *D. lucina* are nocturnal moths and both are attracted to light (26, 27). Both butterfly species are diurnal nectar feeders (28, 29). Moth and butterfly specimens were obtained from wwb.co.uk/ as pupae from May to October 2017, or as dry specimens from www.thebugmaniac.com (March 2018). Tropical pupae (*D. chrysippus*, *G. agamemnon*) were housed in a temperature-controlled cabinet (Economic Deluxe; Snijders Scientific), where they were subject to a 12-h night/day cycle in which temperature varied between 25 and 30 °C while humidity was a constant 70%. Temperate pupae (*A. pernyi*, *D. lucina*) were housed in a laboratory at room temperature and sprayed daily with water. Following eclosion, specimens were killed by freezing them at −18 °C and pinned in a natural position with the wings orientated horizontally to the dorsal plane and allowed to dry at room temperature for 2 wk.

Scale Layer Morphology. Microscopic (Leica EV4W; Leica Microsystems), SEM images (Zeiss Evo15 with Lab6 emitter; Zeiss), and CT sections of each wing sample were used to characterize and compare the scales and scale layers of the species. For SEM images, sections of wing were mounted on adhesive carbon tabs (EM Resolutions) and coated with 5 nm of gold (Quorum Q150R ES; Quorum Technologies). Samples were imaged in both high-vacuum mode using an SE1 detector and variable pressure mode using a VPSE G3 detector. An electron high tension of 15 to 20 kV with 50- to 100-pA probe and a magnification range from ×250 to ×5k were used.

To provide morphological data for modeling, scales from the dorsal surface of the leading and trailing regions of right forewings of the four lepidopteran species were analyzed. Sample size was 10 cover and 10 base scales per wing sample. Measured lengths (from base to tip of individual scale) and width (at widest point) of these 160 scales (*SI Appendix*, Table S1) were then used for numerical scale resonance modeling (see below) to create resonance frequency distributions for each scale array (Fig. 2 *A*–*H*, boxplots). Wing thickness was measured from cross sections as distance between wing membrane and the tip of the furthest most scale. Five measurements were taken from each of the five individuals from each species. All analysis was performed using ImageJ (ImageJ, NIH).

The microscale 3D structure of entire wing samples (Fig. 1*A*, square *Insets*) was measured by synchrotron X-ray CT imaging at the I13-2 Manchester Imaging Branchline at Diamond Light Source. We used pink light, 4× detector, and an exposure time of 15 ms, resulting in a voxel size of 2.6 μm. Nanoscale 3D images of the internal structure of individual scales were obtained by confocal microscopy (TCS SP5; Leica Microsystems). Scale samples were immersed in the mounting medium glycerol. Scales of all four species show the autofluorescence typical for chitin. An excitation wavelength of 488 nm and an emission band of 495 to 720 nm were used to obtain confocal images. The resulting voxel size was 30 × 30 × 80 nm.

We calculated volume fraction of entire lepidopteran wing samples in a two-stage process: First, we analyzed the microscale 3D structure of wing samples by dividing the total number of filled voxels by the total number of voxels measured by summing the numbers of voxels between the first and last filled voxel in each column normal to the wing membrane. Second, we used the nanoscale 3D model of the internal scale structure to determine the volume fraction within each scale. The total volume fraction was the fraction of filled voxels for the wing sample times the volume fraction of the individual scale (*SI Appendix*, Table S3).

Acoustic Tomography. The custom-made acoustic tomography setup consisted of a sensor head comprised of a 1/4″ ultrasound microphone with protective grid removed (type 26AB; GRAS Sound & Vibration A/S), preamplifier (type 2669L), power supply (type 5935-L; both Brüel & Kjær), and a custom-made ring shaped ferro-electret foil loudspeaker (Emfit) driven by a PZD350 M/S high-voltage amplifier (TREK). The microphone was positioned in the central circular opening of the ring speaker (outer radius, 10 mm; hole radius, 4 mm) with speaker and microphone membrane in the same plane and both pointing at the center of the sample. The microphone and speaker acoustic axes were thus coaxial. This sensor head was mounted on an adjustable lever arm moved by a vertically mounted LT360 turntable (LinearX Systems), which allowed the microphone and loudspeaker assembly to move at elevation angles at a resolution of 0.1° with respect to the sample. Microphone, loudspeaker, and turntables were connected to a NI-DAQ BNC-2110 card operated through LabVIEW v.16.0 (both National Instruments) using custom-written scripts.

Two wing areas in each specimen were chosen for tomography, one from the leading and the other from the trailing edge of the forewing about halfway along the wing length (Fig. 1*A*). At these positions, circular sections were punched from whole forewings with a 6-mm-diameter biopsy punch (Kai Medical). Wing samples were mounted at the center of the tomography setup by placing them on a platform (75 × 25 × 300 mm) made of ultrasound absorbing foam (Basotect W; BASF) that is nonreflective across the entire frequency range tested here. A cross line laser (FatMax 77-153; Stanley) was used to align the center of the wing sample with the center of the tomograph. In order to flatten the circular wing sample and to improve

repeatability between treatments, a 1-mm-thick sheet of foam with a central hole of 5-mm diameter was positioned centrally over the wing section. A matching 5-mm diameter hole was present in the foam below the wing, such that 0.5 mm of the wing sample's rim area was clamped and the central 5-mm diameter was exposed on both the dorsal and ventral surfaces.

Acoustic measurements were taken in a 2.9 × 2.7 × 2.3-m semianechoic single-wall audiometric room (IAC Acoustics). Specimens were ensonified with linear frequency modulated sweeps from 250 to 15 kHz of 10-ms duration, covering the range of frequencies used by bats. Sweeps were sampled at 500 kHz with 16-bit resolution. Playback and recordings were sample-synchronous at the same sample rate and resolution.

Echoes from the dorsal surface of each wing sample were acquired from 200-mm distance from 321 different elevation positions (average of five echoes for each direction). For this, the wing sample remained stationary, and the lever arm moved in a semicircular overhead movement in 0.5° steps starting at an elevation of 10° to the horizontal and ending at 170° with the acoustic axis of the sensor head always pointing at the center of the wing sample. The wing samples were positioned such that the scales were aligned parallel to the overhead movement of the sensor head. Echoes of each wing sample were measured in two treatments: "intact" wing sample and "descaled" after all scales had been removed manually using ultrasound absorbing foam fashioned into a pointy tool.

Complex spectral division (pulse forming) with an echo recorded perpendicularly from a 50 × 70-cm metal plate (calibration target) was used to calculate impulse responses. The 321 measured impulse responses were then turned into acoustic tomographies (cross sections through target) using custom-written MATLAB scripts (v9.4; MathWorks; modified after ref. 21).

Acoustic Characterization Based on Tomographies. Acoustic tomographies have the advantage that an area of interest can be selected, and the corresponding echo return analyzed independently from the rest (e.g., background noise, clutter echoes). Here, the wing sample was selected manually in the tomographic image, and subsequent acoustic calculations were based on this area only. The 321 echo impulse responses originating from this area in the tomographic image only were then extracted using inverse radon transforms. Target strength *TS* for a reference distance of 0.1 m was calculated as follows:

$$TS = 10\log_{10}\left(\frac{I_r}{I_i}\right),$$

where I_r and I_i (watts per square meter) are the returned and incident (echo from calibration target) sound intensity, respectively. Spectral target strength is target strength as a function of frequency, which was extracted based on a 2,048-pt fast Fourier transform. We analyzed *TS* for normal sound incidence.

Because I_i was constant, the acoustic effect of scales is the difference in returned sound intensity between intact and descaled wing samples. This acoustic effect could originate from a combination of the following three nonexclusive mechanisms: 1) by increased sound transmission (30), 2) by scattering sound away from the direction of incidence (16, 31), and 3) by sound absorption (5, 6, 15). Sound transmission through the wing sample and diffusion away from the direction of incidence were found to be negligibly small (*SI Appendix*, Figs. S1 and S2) meaning the acoustic effect of scales could be attributed to absorption. The relative absorption coefficient α of the wing scales was hence calculated as sound intensity ratio using the following:

$$\alpha = 1 - \frac{I_{descaled}}{I_{intact}},$$

where I_{intact} and $I_{descaled}$ are the reflected sound intensity of the intact and the descaled wing sample, respectively.

Acoustic Transmission Measurements. Acoustic transmission spectra were measured for intact wing samples of the four lepidopteran species. The experimental setup consisted of a 1/4″ ultrasound microphone with protective grid removed (type 26AB; GRAS Sound and Vibration A/S), preamplifier (type 2669L), power supply (type 5935-L; both Brüel and Kjær), and a custom-made rectangular 10 × 10 mm driven by a high-voltage amplifier (TREK). The loudspeaker and microphone were facing each other from 100-mm distance. An 8-mm wing sample was placed equidistantly between the loudspeaker and the microphone with the dorsal surface facing the loudspeaker. The sample was held in place by a custom-built Perspex brace of 200 × 200 × 20 mm. The brace had a 6-mm diameter hole in the center in which the 8-mm circular wing sample was clamped. This resulted in a circular 6-mm-diameter area of the sample being ensonified. Microphone and loudspeaker were connected to a NI-DAQ BNC-2110 card operated through LabVIEW v.16.0 (both National Instruments) with custom-written code. We played linear frequency sweeps from 250 to 10 kHz and recorded sample-synchronously at 500-kHz sample rate. The transmission coefficient *T* was calculated as sound intensity ratio using the following:

$$T = \frac{T_{wing}}{T_{open}},$$

where T_{wing} is the acoustic transmission measured through an intact wing sample and T_{open} is the transmission when no sample was present (open hole).

Acoustic Diffusion Measurements. Reflected sound fields (*SI Appendix*, Fig. S2) were measured using refractometry following ref. 25, which allows quantitative 2D sound field measurements without the disturbance introduced by the presence of a microphone. We used a scanning laser Doppler vibrometer (LDV) (Polytec PSV-400; POLYTEC) to measure the change in refractive index of a volume of air as acoustic energy was moving through it. The incident sound was a single-period 40-kHz flat wave front (*SI Appendix*, Fig. S2) produced by a custom-made square (70 × 70 mm) ferro-electret foil loudspeaker (Emfit) driven by a high-voltage amplifier (PZD350; TREK). An 8 × 80-mm flat fiberglass reflector was placed 50 mm in front of the speaker. The region between speaker and reflector was scanned at a distance of 50 cm from the LDV lens with scan points spaced 5.5 μm horizontally and 175 μm vertically (*SI Appendix*, Fig. S2). For diffusion comparisons, one measurement was taken with the fiberglass reflector only and another with the reflector covered by a single layer of forewing from *A. pernyi*. The setup was placed on an anti-vibration table (MCI Neuroscience) inside a semianechoic double wall audiometric room (IAC Acoustics).

Changes in sound pressure Δ*P* were calculated following the pressure–refraction relation as in ref. 32, where

$$\frac{\Delta n}{\Delta P} = \beta = 2.68.10^{-9}\ \mathrm{Pa}^{-1},$$

and

$$\Delta P = \frac{\Delta n}{2.68.10^{-9}} = \frac{n}{a}.\frac{\Delta a}{\beta},$$

where Δ*a* is the apparent displacement of a rigid wall given by integrating the LDV velocity output signal and is identical to the magnitude *n* of a modulated path of a laser light traveling through the region and back to the LDV.

Sound diffusion directionality was then quantified from the refractometry measurements by analyzing 173 scan points from a semicircular area 35.5 mm from the center of the reflector. This distance allowed separating the incident from the reflected wave in time. Root-mean-square (rms) of the sound pressure oscillations at each scan point was calculated over the entire reflected wavefront and rms values smoothed by a moving average over 10 consecutive scan points to remove the effect of orthogonal rather than radial scan point distribution. All calculations were performed in MATLAB (v9.4; Mathworks).

Scale Resonance Measurements. To measure their scales' collective vibrational behavior, 2 × 2-mm wing samples from both the leading and trailing edges of the forewings of the four species with ventral scales removed were glued (either water soluble UHU, UHU GmbH, or double-sided tape) onto a cylindrical piezoelectric ultrasound transducer [Fuji Ceramics; Z6T6D-LYX(C-6); diameter = thickness = 6 mm]. The piezo transducer was driven using a high-voltage amplifier (PZD350; TREK) by a frequency sweep from 160 to 20 kHz, and the displacement spectra of a 1 × 1-mm area (scanning grid = 30 × 30 μm) of each wing sample were measured with a scanning Doppler laser vibrometer (LDV; Polytec PSV-400; POLYTEC; point size < 10 μm). LDV, loudspeaker, and samples were mounted on an anti-vibration table (MCI Neuroscience) inside a semianechoic double wall audiometric room (IAC Acoustics). The transfer function of each LDV scanning point was calculated by dividing the velocity spectrum of the scaled wing to the velocity spectrum of the bare piezo, which was used to mount the scaled wing sample on the piezoceramics. Scans for these two conditions were aligned so the sampling points were coincident.

The transfer function represents the velocity on the top surface of the scaled wing relative to the velocity of the piezo at the bottom. Each such transfer function reflects the local resonances at the surface, which are

shaped by the collective vibrational behavior of the local array of scales. *SI Appendix*, Fig. S3 shows a typical transfer magnitude spectrum. As measured transfer spectra are noisy, they were smoothed by Savitzky-Golay filtering. Local maxima with the prominence value higher than 0.4 in *Findpeaks* (MATLAB v9.4; Mathworks) were regarded as resonances. Fig. 2 *A*–*H* shows the distributions of all maxima of all scanning points.

Scale Resonance Modeling. Scale models were built in a multiphysics software (COMSOL v5.3a; COMSOL) for modal analysis. A single scale has three regions, the finger region with five equally spaced fingers, the middle region of uniform width, and the tapering region ending in the stalk, which we assumed to be clamped (*SI Appendix*, Fig. S4). The three regions equally divide the whole scale length. The lengths and widths of the 160 scale models we used are listed in *SI Appendix*, Table S1, and the scale thickness was 4 μm. Stalk width and length and scale thickness were measured for each species based on confocal microscopic images of typical scales (*SI Appendix*, Table S2).

Scale material properties are based on ref. 5 with density = 559 kg/m^3 and the following effective stiffness matrix:

$$\text{Stiffness matrix} = \begin{pmatrix} c_{11} & c_{12} & c_{13} & & & \\ c_{12} & c_{22} & c_{23} & & 0 & \\ c_{13} & c_{23} & c_{33} & & & \\ & & & c_{44} & 0 & 0 \\ & 0 & & 0 & c_{55} & 0 \\ & & & 0 & 0 & c_{66} \end{pmatrix}$$

$$= \begin{pmatrix} 21.89 & 2.88 & 2.15 & 0 & 0 & 0 \\ 2.88 & 11.5 & 1.21 & 0 & 0 & 0 \\ 2.15 & 1.21 & 8.06 & 0 & 0 & 0 \\ 0 & 0 & 0 & 2.78 & 0 & 0 \\ 0 & 0 & 0 & 0 & 1.13 & 0 \\ 0 & 0 & 0 & 0 & 0 & 1.36 \end{pmatrix} \times \text{GPa},$$

with direction 1 being the long axis of the scale; direction 2, its width; and direction 3, the scale thickness. The first six resonances of each scale were calculated, and the static frequency distribution of all 160 scales is shown as boxplots in Fig. 2 *A*–*H*.

Mixed Scale Array Absorption Modeling. A unit cell model containing a 4 × 4 scale was built in COMSOL to quantify the effect of mixing scales of different resonances on the absorption of the scale array (Fig. 3). A quadratic tetrahedral element was used for the modeling. The maximum element size was 30 μm, resulting in a wavelength/element size ratio of 208.33 for an example frequency of 55 kHz (wavelength, 6.25 mm). The model was assigned Floquet periodic boundaries, which expand the 16-element unit cell to an infinitely repeating 2D array. All 16 scales were identical in morphology at 300 μm long, 150 μm wide, and 4 μm thick. The scales were arranged in a 185 × 185-μm grid, which makes neighboring scale rows overlap longitudinally to a similar degree to that observed in the moths. All scales were inserted at a 25-degree angle into the wing membrane consisting of a 3-μm-thick solid chitin layer with a Young's modulus = 65 GPa, Poisson's ratio = 0.35, and density = 1,300 kg/m^3. Scale material properties were as detailed in *Scale Resonance Modeling* above. The scale diversity is realized by setting different stiffness scaling factors for each scale (Fig. 3, *Right Inset*).

The transmission coefficient R_Π, reflection coefficient T_Π, and absorption coefficient α of the scale array were calculated by the following formulae:

$$R_\Pi = |p_r|^2 / |p_i|^2,$$

$$T_\Pi = |p_t|^2 / |p_i|^2,$$

$$\alpha = 1 - R_\Pi - T_\Pi,$$

where p_r is the reflected sound pressure, p_i is the incident sound pressure, and p_t is the transmitted sound pressure. The incident and reflected sound pressure values were derived by averaging the numerically calculated pressure on a plane above the array, and the transmitted pressure value was calculated by averaging the calculated pressure on a plane below the array.

Scale Coupling Modeling. Individual scales are attached to the common flexible wing membrane and hence mechanically coupled. Certain graded resonator metamaterials also use common substrate coupling to achieve collective vibrational behavior (24). Scale coupling in the moth wing was verified numeric ally by comparing the calculated displacement spectra of individual scales in two uniform scale arrays and one mixed scale array (*SI Appendix*, Fig. S5). In the two uniform arrays, the scales' stiffness matrices have either been multiplied by a scaling factor of 1.2 (type A) or 1.6 (type B). In the mixed array, rows of scales were alternatingly multiplied by a scaling factor of 1.2 or 1.6. Scale displacement was measured as the vertical displacement amplitude of the scale tip relative to the scale stalk during the oscillation. Displacement spectra show a single peak for the two uniform scale arrays, while when mixing the two scales together, the displacement peaks of both scale shift. For the scale type A in the mixed array, a second displacement peak corresponding to the resonance of the scale type B appears.

Statistical Analysis. Repeated-measures *t* tests (two-tail) were used to compare differences in target strengths among treatments as a function of frequency. An ANOVA was used to test for differences in scale and wing morphologies across species, and Tukey–Kramer post hoc tests were used for pairwise comparisons. All statistical analysis was performed using a commercial statistical analysis package (RStudio, Version 0.99.473; RStudio).

Data Availability. Echo spectra data have been deposited in the University of Bristol research data repository, http://data.bris.ac.uk/data/dataset/l7qg341nfpe92uy4qp9pxjqwj (33).

ACKNOWLEDGMENTS. We thank Christoph Rau, Shashi Marathe, and Kaz Wanelik from beamline I13 at Diamond Light Source for their invaluable assistance. We thank Aila Osborne and Alexander Quinn for help with measuring transmission coefficients. This study was supported by the Biotechnology and Biological Sciences Research Council (Grants BB/N009991/1 and BB/I009671/1), the Engineering and Physical Sciences Research Council (Grant EP/T002654/1), and Diamond Light Source, beamline I13 (proposal MT17616).

1. M. Yang, P. Sheng, Sound absorption structures: From porous media to acoustic metamaterials. *Annu. Rev. Mater. Res.* **47**, 83–114 (2017).
2. Z. Liu *et al*., Locally resonant sonic materials. *Science* **289**, 1734–1736 (2000).
3. P. Wang, F. Casadei, S. Shan, J. C. Weaver, K. Bertoldi, Harnessing buckling to design tunable locally resonant acoustic metamaterials. *Phys. Rev. Lett.* **113**, 014301 (2014).
4. S. Zhang, C. Xia, N. Fang, Broadband acoustic cloak for ultrasound waves. *Phys. Rev. Lett.* **106**, 024301 (2011).
5. Z. Shen, T. R. Neil, D. Robert, B. W. Drinkwater, M. W. Holderied, Biomechanics of a moth scale at ultrasonic frequencies. *Proc. Natl. Acad. Sci. U.S.A.* **115**, 12200–12205 (2018).
6. T. R. Neil, Z. Shen, D. Robert, B. W. Drinkwater, M. W. Holderied, Thoracic scales of moths as a stealth coating against bat biosonar. *J. R. Soc. Interface* **17**, 20190692 (2020).
7. H. M. Ter Hofstede, J. M. Ratcliffe, Evolutionary escalation: The bat-moth arms race. *J. Exp. Biol.* **219**, 1589–1602 (2016).
8. K. D. Roeder, *Nerve Cells and Insect Behavior* (Harvard University Press, 1998).
9. L. Acharya, M. B. Fenton, Bat attacks and moth defensive behaviour around street lights. *Can. J. Zool.* **77**, 27–33 (1999).
10. W. E. Conner, "Adaptive sounds and silences: Acoustic anti-predator strategies in insects" in *Insect Hearing and Acoustic Communication*, B. Hedwig, Ed. (Springer, 2014), pp. 65–79.
11. L. J. O'Reilly, D. J. L. Agassiz, T. R. Neil, M. W. Holderied, Deaf moths employ acoustic Müllerian mimicry against bats using wingbeat-powered tymbals. *Sci. Rep.* **9**, 1444 (2019).
12. J. G. J. E. Kingsolver, Thermoregulation and flight in *Colias* butterflies: Elevational patterns and mechanistic limitations. *Ecology* **64**, 534–545 (1983).
13. T. Eisner, R. Alsop, G. Ettershank, Adhesiveness of spider silk. *Science* **146**, 1058–1061 (1964).
14. P. M. Brakefield, T. G. Liebert, Evolutionary dynamics of declining melanism in the peppered moth in The Netherlands. *Proc. R. Soc. Lond. B.* **267**, 1953–1957 (2000).
15. J. Zeng *et al*., Moth wing scales slightly increase the absorbance of bat echolocation calls. *PLoS One* **6**, e27190 (2011).
16. N. Jiménez, T. J. Cox, V. Romero-García, J.-P. Groby, Metadiffusers: Deep-subwavelength sound diffusers. *Sci. Rep.* **7**, 5389 (2017).
17. G. Ma, M. Yang, S. Xiao, Z. Yang, P. Sheng, Acoustic metasurface with hybrid resonances. *Nat. Mater.* **13**, 873–878 (2014).
18. M. Yang, S. Chen, C. Fu, P. Sheng, Optimal sound-absorbing structures. *Mater. Horiz.* **4**, 673–680 (2017).
19. P. Celli, B. Yousefzadeh, C. Daraio, S. Gonella, Bandgap widening by disorder in rainbow metamaterials. *Appl. Phys. Lett.* **114**, 091903 (2019).
20. J. Zhu *et al*., Acoustic rainbow trapping. *Sci. Rep.* **3**, 1728 (2013).
21. H. Meng, D. Chronopoulos, A. T. Fabro, I. Maskery, Y. Chen, Optimal design of rainbow elastic metamaterials. *Int. J. Mech. Sci.* **165**, 105185 (2020).
22. G. J. Chaplain, D. Pajer, J. M. De Ponti, R. V. Craster, Delineating rainbow reflection and trapping with applications for energy harvesting. *New J. Phys.* **22**, 1–12 (2020).
23. A. Colombi, D. Colquitt, P. Roux, S. Guenneau, R. V. Craster, A seismic metamaterial: The resonant metawedge. *Sci. Rep.* **6**, 27717 (2016).

24. E. Skelton, R. Craster, A. Colombi, D. Colquitt, The multi-physics metawedge: Graded arrays on fluid-loaded elastic plates and the mechanical analogues of rainbow trapping and mode conversion. *New J. Phys.* **20**, 053017 (2018).
25. D. Cardella, P. Celli, S. Gonella, Manipulating waves by distilling frequencies: A tunable shunt-enabled rainbow trap. *Smart Mater. Struct.* **25**, 085017 (2016).
26. F. Barsics, T. M. Razafimanantsoa, J. Minet, É. Haubruge, F. Verheggen, "Nocturnal moth inventory in Malagasy tapia woods, with focus on silk-producing species" in *Les Vers à Soie Malgaches. Enjeux Écologiques et Socio-économiques*, F. Verheggen, J. Bogaert, E. Haubruge, Eds. (Les Presses Agronomiques de Gembloux, Gembloux, Belgium, 2013), pp. 77–89.
27. C. Lemaire, J. Minet, "The Bombycoidea and their relatives" in *Lepidoptera, Moths and Butterflies. Volume 1: Evolution, Systematics, and Biogeography*. Handbook of Zoology, Volume IV, Part 35, N. P. Kristensen, Ed. (W. de Gruyter, Berlin, 1998), pp. 321–353.
28. S. P. Ramana, J. B. Atluri, C. S. Reddi, Autecology of the tailed jay butterfly *Graphium agamemnon* (Lepidoptera : Rhopalocera : Papilionidae). *J. Environ. Biol.* **24**, 295–303 (2003).
29. D. Smith, Batesian mimicry between *Danaus chrysippus* and *Hypolimnas misippus* (Lepidoptera) in Tanzania. *Nature* **242**, 129–131 (1973).
30. X. Jing, X. Wang, X. Sun, Broadband acoustic liner based on the mechanism of multiple cavity resonance. *AIAA J.* **45**, 2429–2437 (2007).
31. T. J. Cox, P. D'antonio, *Acoustic Absorbers and Diffusers: Theory, Design and Application* (CRC Press, 2009).
32. R. Malkin, T. Todd, D. Robert, Quantitative imaging of acoustic reflection and interference. *J. Physics Conf. Ser.* **581**, 012007 (2015).
33. M. W. Holderied, Z. Shen, T. R. Neil, Data from Physics of Life (10-2020). data.bris Research Data Repository. https://data.bris.ac.uk/data/dataset/l7qg341nfpe92uy4qp9pxjqvj. Deposited 13 October 2020.